

# Exploring the photometric signatures of magnetospheres around helium-strong stars

R. H. D. Townsend\*

*Bartol Research Institute, Department of Physics and Astronomy, University of Delaware, Newark, DE 19716, USA*

Accepted 2008 May 7. Received 2008 April 20; in original form 2007 August 30

## ABSTRACT

Photometric variations due to magnetically confined material around helium-strong stars are investigated within the framework of the rigidly rotating magnetosphere model. For dipole field topologies, the model is used to explore how the morphology of light curves evolves in response to changes to the observer inclination, magnetic obliquity, rotation rate and optical depth. The general result is that double-minimum light curves arise when the obliquity and/or inclination are close to  $90^\circ$ ; no light variations are seen in the opposite limit. For intermediate cases, single-minimum light curves occur. These findings are interpreted with the aid of a simple, analytical torus model, paving the way for the development of new photometric-based constraints on the fundamental parameters of helium-strong stars. Illustrative applications to five stars in the class are presented.

**Key words:** techniques: photometric – stars: chemically peculiar – stars: fundamental parameters – stars: magnetic fields – stars: rotation – stars: variables: other.

## 1 INTRODUCTION

Helium-strong (He-strong) stars are a small class of chemically peculiar B stars, interpreted as an extension of the Ap/Bp phenomenon to higher effective temperatures (Osmer & Peterson 1974). They are characterized by elevated and spatially inhomogeneous photospheric He abundances, and in most cases also exhibit strong magnetic fields (see Bohlender et al. 1987, and references therein). Spectroscopy of their time-varying He absorption lines often reveals that the surface abundance distribution is strongly correlated with field topology (Bohlender & Landstreet 1988; Veto 1990). These correlations lend support to models for the abundance anomalies that rely on the interplay between radiative and magnetic forces, either in the framework of elemental diffusion (e.g. Michaud 1970), or in the context of wind mass loss (e.g. Hunger & Groote 1999).

Of the He-strong stars exhibiting photometric variability (Pedersen & Thomsen 1977), at least some can be successfully explained by invoking rotational modulation of the visible abundance inhomogeneities – so-called ‘spot’ models (see, for example, Krtićka et al. 2007). However, a different approach is required for other objects in the class, most notably the B2pe star  $\sigma$  Ori E. The light curve of this star has a double-eclipse morphology (Hesser, Ugarte & Moreno 1977), leading some authors (e.g. Hesser, Walborn & Ugarte 1976) initially to suggest that the star is a mass-transfer binary. In fact, as further observational data have become available, an empirical picture for the star’s photometric and spec-

troscopic variability has emerged (Groote & Hunger 1982) that augments a spot model with a pair of circumstellar clouds. These clouds absorb continuum photons as they transit the stellar disc, giving rise to the distinctive photometric minima; however, once off the disc they reveal themselves in  $H\alpha$  line profiles as blueshifted and redshifted emission components (e.g. Walborn & Hesser 1976; Pedersen 1979).

Recently, Townsend & Owocki (2005, hereafter TO-05) have developed a rigidly rotating magnetosphere (RRM) model that provides the theoretical basis for this empirical picture. The model conjectures that plasma in the star’s radiatively driven wind, channelled by nearly rigid field lines, tends to accumulate at points where the effective (gravitational plus centrifugal) potential is at a local minimum. This steady accumulation leads to the development of a magnetosphere resembling a warped disc, which is supported by the centrifugal force and corotates rigidly with the star. For an oblique dipole field topology, the RRM model predicts that the magnetospheric density is highest in two regions – ‘clouds’ – situated along the twin intersections between the magnetic and rotational equators. In the specific case of  $\sigma$  Ori E, the photometric and  $H\alpha$  variations synthesized using the model show very good agreement with observations of the star (Townsend, Owocki & Groote 2005).

In this paper, I apply the RRM model in a broader context, by exploring how the photometric signatures of magnetospheric plasma depend on fundamental parameters such as the observer inclination and magnetic obliquity (Section 2). The results from this parameter-space exploration are interpreted with the aid of a simple, analytical torus model (Section 3), and I discuss how they might be applied to

\*E-mail: rhd@bartol.udel.edu

constrain the parameters of He-strong stars (Section 4). The principal findings are then summarized (Section 5).

## 2 EXPLORATION OF PARAMETER SPACE

### 2.1 Light-curve synthesis

The RRM model, as applied to a dipole magnetic topology, is used to synthesize the light curves used for exploring parameter space. The same procedure described by Townsend et al. (2005, their section 3.2) is followed; note, therefore, that the variability arising from abundance inhomogeneities is not considered. It is assumed that there is no decentering of the magnetic field,  $\mathbf{a} = \mathbf{0}$  (Townsend et al. 2005, equation 1), and a canonical energy ratio parameter  $\epsilon_* = 10^{-3}$  (cf. TO-05, equation 38) is adopted throughout.

The remaining free parameters of the model are then the inclination  $i$ , the magnetic obliquity  $\beta$ , the ratio

$$\omega = \frac{\Omega}{\Omega_c} \quad (1)$$

between the rotation frequency  $\Omega$  and the critical frequency  $\Omega_c$ , and an optical depth scale

$$\tau_0 = \frac{\kappa \dot{M} t \omega^{4/3}}{R_*^2}. \quad (2)$$

This latter expression groups the opacity  $\kappa$  (assumed spatially constant) with various terms appearing in the RRM prescription for the density (TO-05, equation 35). The additional  $\omega^{4/3}$  term comes from considering the rotational dependence of the total magnetospheric mass column between star and observer; its inclusion ensures that models having the same  $\tau_0$  but differing  $\omega$  exhibit approximately the same degree of light variations.

### 2.2 Varying $\beta$ and $i$

To begin the exploration of parameter space, a grid of light curves is synthesized in  $5^\circ$  increments over the full intervals  $0^\circ \leq i \leq 90^\circ$  and  $0^\circ \leq \beta \leq 90^\circ$ . In each case, an intermediate rotation rate of  $\omega = 0.5$  is assumed, and an optical depth scale  $\tau_0 = 10$  is chosen to produce variability on the  $\sim 10$  per cent level typical to He-strong stars. Fig. 1 illustrates the resulting light curves, plotting the flux  $F$  (in units of the unobscured stellar flux  $F_*$ ) against the rotational phase  $\phi$ .<sup>1</sup> For clarity, only the curves at even multiples of  $5^\circ$  are shown, and the  $i < 30^\circ$  cases are omitted because none exhibits any significant variability.

The figure clearly demonstrates how the character of the light curves is altered as  $i$  and  $\beta$  are changed. In the limit where either of these parameters is large, the curves exhibit a clear double-minimum (hereafter, ‘2-m’) morphology. In the opposite limit, and in particular for  $i < 30^\circ$  as already mentioned, a non-varying, constant morphology (‘0-m’) is seen. For intermediate cases, falling approximately along a band extending from  $\{i, \beta\} = \{30^\circ, 90^\circ\}$  to  $\{i, \beta\} = \{90^\circ, 0^\circ\}$ , a single light minimum (‘1-m’) occurs at phase  $\phi = 180^\circ$ .

To understand the origin of these three morphologies, Fig. 2 shows maps of the column density  $D$  in the near-star regions of the circumstellar environment, for three configurations having  $\beta = 50^\circ$  and

$i = 30^\circ, 50^\circ$  and  $90^\circ$ . The maps are calculated from an expression of the form

$$D(x_o, y_o) = \int \rho(x_o, y_o, z_o) dz_o, \quad (3)$$

where  $(x_o, y_o, z_o)$  are Cartesian coordinates in the observer’s reference frame, with  $z_o$  directed toward the observer, and  $\rho$  is the local density predicted by the RRM model (cf. TO-05, equation 35). Fig. 2(a), which plots the  $i = 30^\circ$  case, is typical of low-inclination systems. With the observer situated close to the rotation pole, the plasma trapped in the magnetosphere – lying in a disc between the rotational and magnetic equatorial planes – has no opportunity to pass between the observer and the star. Hence, an unvarying, 0-m light curve is seen in these systems.

For Fig. 2(c), the converse is true. With the observer in the rotational equatorial plane, the magnetospheric plasma transits the star twice per rotation cycle, and thus a 2-m light curve arises. In this particular case, symmetry requires that the minima occur at phases  $\phi = 90^\circ$  and  $270^\circ$ , with a half-cycle difference between them. However, as discussed in further detail below, a smaller phase difference  $\Delta\phi$  is found for 2-m configurations having  $i < 90^\circ$  and  $\beta < 90^\circ$ .

Fig. 2(b) illustrates the intermediate,  $i = 50^\circ$  case, where the observer is not sufficiently close to the rotational equator for magnetospheric plasma to pass fully in front of the star. Instead, when the magnetic field is pointed away from the observer, the plasma grazes the lower portions of the stellar limb, causing a 1-m light curve with the minimum centred at phase  $\phi = 180^\circ$ . This light curve is characterized by a reduced overall absorption, relative to the 2-m case shown in Fig. 2(c).

As can be seen from the  $\beta = 50^\circ$  row of light curves in Fig. 1, a smooth evolutionary sequence links the cases shown in Figs 2(a)–(c). As the observer moves from the rotational equator toward smaller  $i$ , the depth ( $\equiv F_* - F$ ) at the twin light minima of the (initially, 2-m) light curve decreases, whereas the depth at the intervening light maximum at  $\phi = 0.5$  increases. Eventually, these depth values cross over, with the result that the light curve transitions to a 1-m morphology. Following this switch-over (which, in the  $\beta = 50^\circ$  case, occurs at  $i \approx 60^\circ$ ), the depth at the single remaining minimum at  $\phi = 180^\circ$  declines toward lower  $i$ , and eventually vanishes in a further transition to a 0-m morphology.

The progressive distortion of light curves, as the 2-m to 1-m transition is approached, has an influence on the phase difference  $\Delta\phi$  between the minima. To explore this influence, each light curve in the  $i$ – $\beta$  grid is analysed using a simple algorithm that determines its morphology, and – if 2-m – measures the phase difference. The algorithm involves three steps, as follows.

- (i) If the total flux variation  $\Delta F \equiv \max(F) - \min(F)$  is less than  $0.01 F_*$ , then the light curve is classified as 0-m.
- (ii) Otherwise, if the light curve exhibits two flux minima, and these minima are separated by flux maxima that both satisfy  $F - \min(F) > 0.15 \Delta F$ , then the light curve is classified as 2-m.
- (iii) Otherwise, the light curve is classified as 1-m.

A minor complication arises when minima are cusped (see Section 2.3 and Fig. 4). Then, the adopted phase of a minimum is determined by averaging the phases of the local minima on either side of the cusp.

Fig. 3 plots the results of this analysis, showing the  $\Delta\phi$  values for the 2-m light curves in the  $i$ – $\beta$  plane, and also indicating where in the plane 1-m and 0-m curves occur. (The middle panel of the figure shows the  $\omega = 0.5$  case considered in this section. The other two panels, corresponding to  $\omega = 0.25$  and  $\omega = 0.75$ , are discussed in

<sup>1</sup> In the present work,  $\phi = 0^\circ$  corresponds to magnetic maximum. This differs from the convention adopted by Townsend et al. (2005), who followed historical precedent (e.g. Hesser et al. 1977) by choosing the primary light minimum as phase zero.

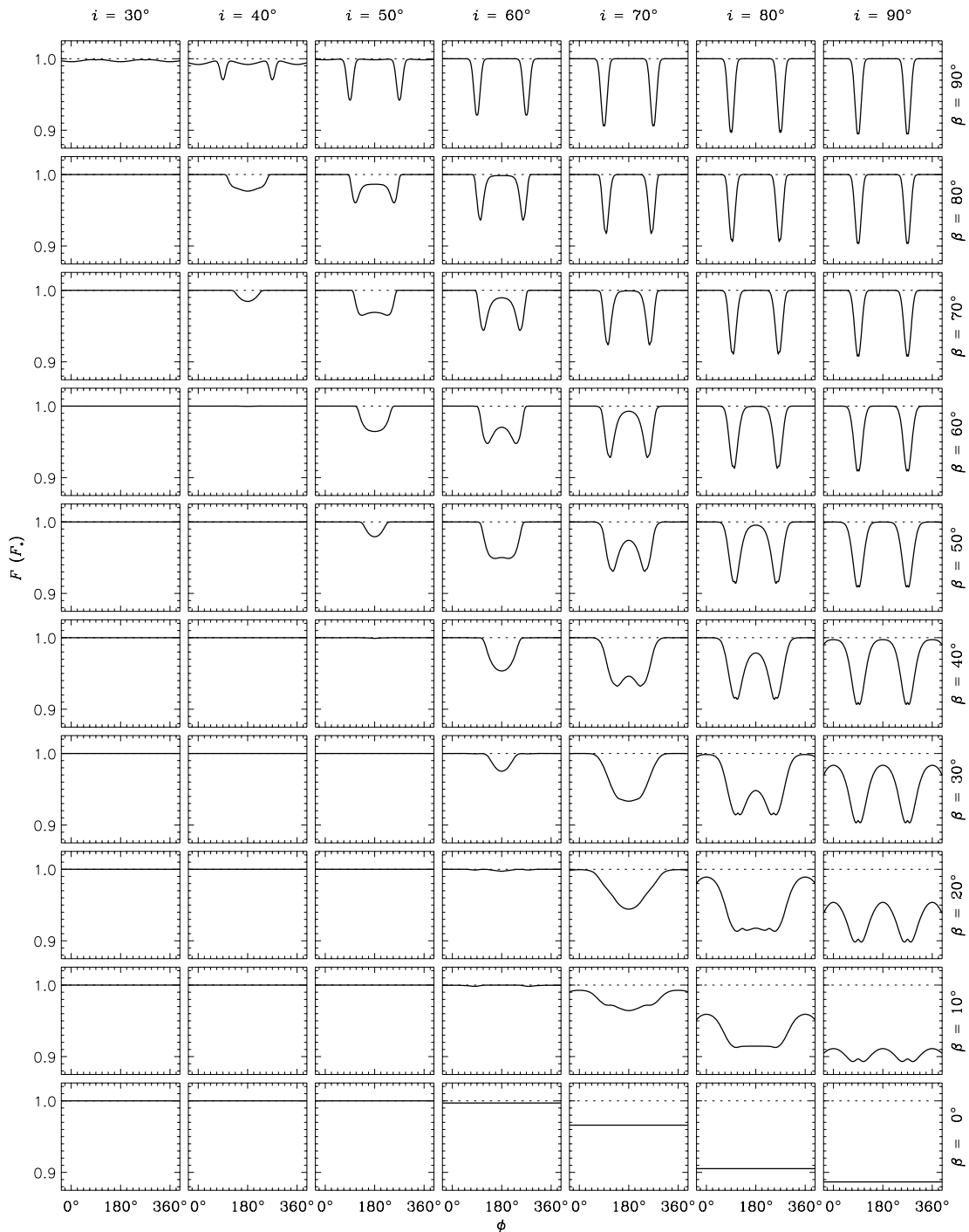


**Figure 1.** Light curves synthesized with varying inclination  $i$  and obliquity  $\beta$ , in each case plotting the flux  $F$  (in units of the unobscured stellar flux  $F_*$ ) as a function of the rotation phase  $\phi$ ; a rotation rate  $\omega = 0.5$  and an optical depth scale  $\tau_0 = 10$  are assumed. The dotted horizontal lines indicate the level  $F = F_*$ .

the following section.) As before, the  $i < 30^\circ$  region of the plane is uniformly 0-m and is therefore not shown. However, in the present case the  $\beta < 20^\circ$  region is also omitted, because there the analysis algorithm gives unreliable results. This is more because of the difficulty in sensibly classifying the light curves in this region (in particular, see the  $\{i, \beta\} = \{80^\circ, 10^\circ\}$  and  $\{90^\circ, 10^\circ\}$  cases shown in Fig. 1) than to any particular limitation of the algorithm.

The figure confirms the previous finding that the 0-m and 2-m light curves are situated toward small and large angles, respec-

tively, with the 1-m curves falling in between. However, it also reveals that  $\Delta\phi$  depends quite regularly on  $i$  and  $\beta$ . When either of these parameters is equal to  $90^\circ$ , the phase difference is exactly one-half of a cycle; as already mentioned, this is required by symmetry. Away from these special cases, and toward the boundary between the 2-m and 1-m regions,  $\Delta\phi$  is constant along contours running from the low- $i$ /high- $\beta$  corner down to the high- $i$ /low- $\beta$  corner. The origin of this behaviour is explored further in Section 3.

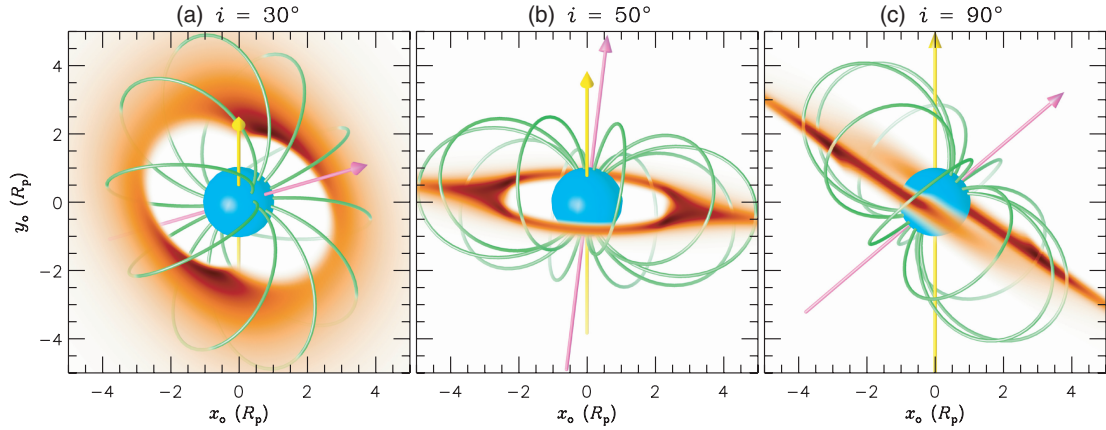


**Figure 2.** Maps of the column density  $D$  in the observer’s image plane  $(x_o, y_o)$ , for three RRM configurations: (a)  $\{i, \beta\} = \{30^\circ, 50^\circ\}$  at a rotational phase  $\phi = 81^\circ$ ; (b)  $\{i, \beta\} = \{50^\circ, 50^\circ\}$  at  $\phi = 171^\circ$ ; (c)  $\{i, \beta\} = \{90^\circ, 50^\circ\}$  at  $\phi = 81^\circ$ . (The phases are offset slightly from the ‘round-number’ values  $90^\circ$  and  $180^\circ$ , to improve visual clues to the three-dimensional geometry.) In all three cases,  $\omega = 0.5$ . Black/opaque corresponds to the highest column density, and white/transparent to the lowest, with intermediate levels shown in orange. The central star is coloured blue, and the axes are drawn as arrows: yellow/upright for the rotation axis and magenta/oblique for the magnetic axis. Moreover, selected field lines with a summit radius of  $5R_p$  (where  $R_p$  is the stellar radius at the rotational poles) are indicated in green.

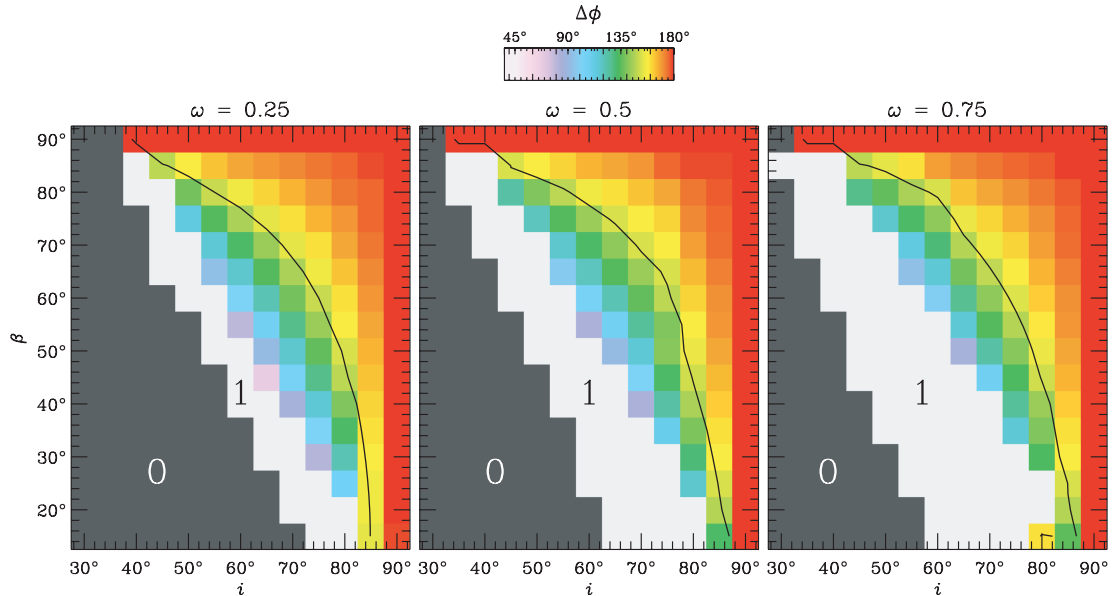


**Figure 3.** The phase difference  $\Delta\phi$  between the minima in 2-m light curves, plotted in the  $i$ - $\beta$  plane for three differing rotation rates; in every case,  $\tau_0 = 10$ . The curve in each panel shows the contour  $\Delta\phi = 150^\circ$ , discussed in Section 4.2.2. The regions of the plane associated with 0-m and 1-m curves are shown in monochrome and labelled as ‘0’ and ‘1’, respectively.

### 2.3 Varying $\omega$

The three panels of Fig. 3, showing the light-curve morphologies in the  $i$ - $\beta$  plane for  $\omega = 0.25, 0.5$ , and  $0.75$ , illustrate some of the effects of varying the rotation rate. The most obvious trend is the expansion of the 1-m region as  $\omega$  is increased. This comes almost entirely at the expense of the 0-m region; almost no change is seen in the 2-m region, either in terms of its extent, or in terms of the  $\Delta\phi$  values shown. Again, the reasons for such behaviour are explored further in Section 3.

Focusing now on an individual case, Fig. 4 plots the light curves for a  $\{i, \beta\} = \{70^\circ, 50^\circ\}$  configuration [chosen as halfway between the cases shown in Figs 2(b) and (c)], synthesized for the same three  $\omega$  values above. As already noted for Fig. 3, the rotation rate has only a minor impact on the phase difference between the light

minima; the measured differences are  $\Delta\phi = 118^\circ$  for  $\omega = 0.25$ ,  $\Delta\phi = 116^\circ$  for  $\omega = 0.50$ , and  $\Delta\phi = 124^\circ$  for  $\omega = 0.75$ , amounting to only a  $\sim 10$  per cent variation from a factor of 3 increase in  $\omega$ .

However, a significant increase occurs in the width of the individual light minima toward more rapid rotation. This indicates that the magnetospheric plasma is taking relatively longer to transit across the star, and follows from the approximate scaling of the RRM inner-edge radius with the Kepler radius,

$$R_K = \frac{3R_p}{2\omega^{2/3}} \quad (4)$$

(cf. TO-05, equation 12). As  $\omega$  increases, both  $R_K$  and the inner edge move in towards the star. Thus, the plasma takes a larger

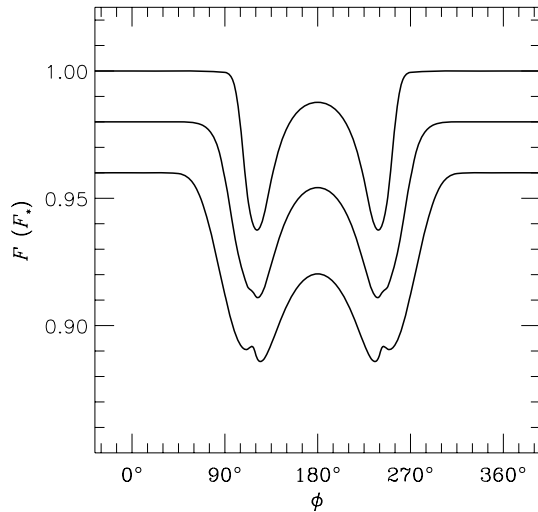


**Figure 4.** Light curves for a  $\{i, \beta\} = \{70^\circ, 50^\circ\}$  configuration, synthesized with  $\tau_0 = 10$  and rotation rates  $\omega = 0.25, 0.50$  and  $0.75$ . For clarity, the  $\omega = 0.50$  curve is displaced downward by  $0.02 F_*$ , and the  $\omega = 0.75$  curve by  $0.04 F_*$ .

fraction of a rotation cycle to transit, and broader light minima ensue.

An additional effect of rapid rotation, seen in the  $\omega = 0.75$  curve of Fig. 4, is to produce cusping at the minima of the light curve. This effect, which is the characteristic hallmark of an optically thick yet geometrically thin disc, arises because the scaleheight  $h_m$  of the disc-like magnetosphere varies as  $\sim R_K^{3/2} \sim \omega^{-1}$  (cf. TO-05, equation 29).

#### 2.4 Varying $\tau_0$

For the sake of completeness, Fig. 5 plots the light curves for the same  $\{i, \beta\} = \{70^\circ, 50^\circ\}$  configuration considered previously, but synthesized this time with a fixed rotation rate  $\omega = 0.50$  and varying optical depth scale:  $\tau_0 = 5, 10$  and  $15$ . The maximum depths of the light curves ( $0.037 F_*$ ,  $0.069 F_*$  and  $0.099 F_*$ , respectively) increase

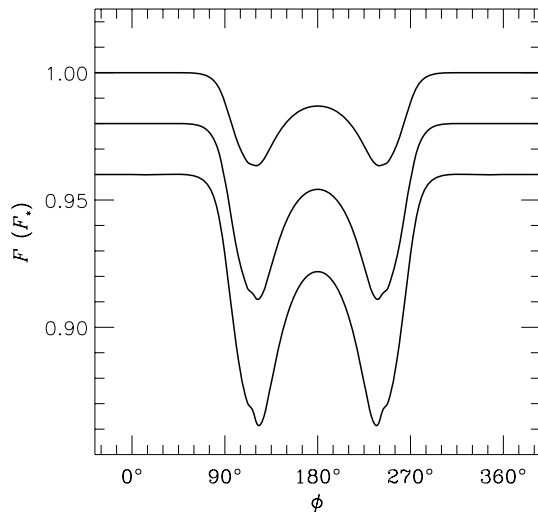


**Figure 5.** Light curves for a  $\{i, \beta\} = \{70^\circ, 50^\circ\}$  configuration, synthesized for  $\omega = 0.50$  and optical depth scales  $\tau_0 = 5, 10$  and  $15$ . For clarity, the  $\tau_0 = 10$  curve is displaced downward by  $0.02 F_*$ , and the  $\tau_0 = 15$  curve by  $0.04 F_*$ .

approximately linearly with  $\tau_0$ . This result is a natural consequence of the fact that the magnetospheric densities (cf. TO-05, equation 35) are proportional to  $\tau_0$ . As in the preceding section, however, the change in phase difference is small: in the direction of increasing  $\tau_0$ ,  $\Delta\phi = 120^\circ, 116^\circ$  and  $114^\circ$ .

### 3 A TORUS MODEL

The previous sections explore how RRM light-curve morphology is sensitive to parameters such as  $i, \beta$  and  $\omega$ . A number of interesting dependences emerge, as seen for instance in Fig. 3. To gain a measure of insight into these dependences, the present section introduces an idealized, analytical torus model for the formation of the light curves.

In this model, flux variations arise as a result of obscuration of a spherical star by an optically thick, oblique, corotating torus of circumstellar material. Assuming that the torus is narrow compared to the stellar radius, the observed flux at any instant can be approximated by considering the fraction of the stellar disc obscured:

$$F = F_* \left( 1 - \frac{\ell d_t}{\pi R_*^2} \right). \quad (5)$$

Here,  $R_*$  is the stellar radius,  $d_t (\ll R_*)$  is the torus cross-sectional diameter and  $\ell$  is the length of the torus arc (if any) covering the stellar disc. For a torus radius  $R_t$  sufficiently larger than the stellar radius  $R_*$ , this arc length is approximated by

$$\ell \approx 2\sqrt{\max(R_*^2 - b^2, 0)}, \quad (6)$$

where  $b$  is the semimajor axis of the ellipse that is the projection of the torus on the plane of the sky (see Fig. 6). If the torus plane is tilted by an angle  $\nu_t$  to the rotation axis, it can be shown that

$$b = R_t |\cos i \cos \nu_t + \sin i \sin \nu_t \cos \phi|. \quad (7)$$

Even before light curves are synthesized, these expressions can be used to confirm that the torus model reproduces the same three light-curve morphologies found previously. For any light variations

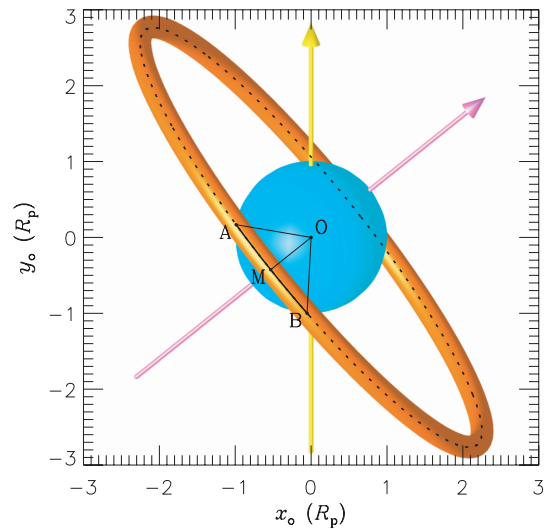


**Figure 6.** Torus model for a  $\{i, \nu_t, R_t\} = \{70^\circ, 50^\circ, 3.5 R_p\}$  configuration, seen at rotational phase  $\phi = 92^\circ$ ; the torus is coloured orange, while the star and axes are as in Fig. 2. The dotted line shows the ellipse corresponding to the sky projection of the torus; this ellipse is centred at point O, and intersects the stellar limb at points A and B. The arc AB has length  $\ell$ , and the line OM (where M is the midpoint of the arc) is the semiminor axis  $b$  of the ellipse.

whatsoever to occur,  $b$  must be smaller than  $R_*$  at some point during the rotation cycle. Assuming that  $0^\circ \leq i \leq 90^\circ$  and  $0^\circ \leq \nu_t \leq 90^\circ$ , this is equivalent to the requirement

$$\cos(i + \nu_t) < \frac{R_*}{R_t}. \quad (8)$$

If this condition is fulfilled, then the light curve exhibits a 1-m or 2-m morphology depending on whether the torus passes across the centre of the stellar disc:

$$\cos(i + \nu_t) \begin{cases} > 0 & \text{1-m} \\ < 0 & \text{2-m} \end{cases}. \quad (9)$$

In the 1-m case, the flux minimum always occurs at phase  $\phi = 180^\circ$ . In the 2-m case, the minima arise when

$$\cos i \cos \nu_t = -\sin i \sin \nu_t \cos \phi, \quad (10)$$

so that the phase difference is given by

$$\Delta\phi = 2 \cos^{-1}(\cot i \cot \nu_t). \quad (11)$$

A similar expression has been derived by Shore & Brown (1990, their equation 2), but in their case  $\beta$  appears in the place of  $\nu_t$ .

To now relate the foregoing analysis back to the RRM model, representative values are chosen for the torus radius  $R_t$  and tilt angle  $\nu_t$ . For the former, the Kepler radius  $R_K$  (cf. equation 4) is the appropriate choice; for the latter, it is argued in Appendix A that

$$\nu = \beta - \tan^{-1} \left( \frac{\sin 2\beta}{5 + \cos 2\beta} \right) \quad (12)$$

furnishes a good characterization of the mean tilt of the magnetospheric disc. Adopting these values, and further assuming a diameter  $d_t = 0.1R_*$ , equations (5)–(7) are used to synthesize a  $\beta$ – $i$ – $\omega$  grid of light curves. These data are analysed using the algorithm described in Section 2.2, and Fig. 7 plots the results in the same format as Fig. 3.

The two figures show a good measure of qualitative agreement. Specific characteristics of the RRM model that are correctly reproduced by the torus model include the following:

(i) the three differing light-curve morphologies (0-m, 1-m and 2-m), and their general locations in the  $\{i, \beta\}$  plane;

(ii) the fact that the phase differences of 2-m light curves are insensitive to rotation rate (this follows from equation 11, which has no dependence – explicit or implicit – on  $\omega$ );

(iii) likewise, the fact that the boundary between the 1-m and 2-m regions is insensitive to the rotation rate (this follows from equation 9, which again has no dependence on  $\omega$ );

(iv) conversely, the fact that the boundary between the 0-m and 1-m regions does depend on the rotation rate, moving toward lower  $i$  as  $\omega$  is increased (this is because of the identification  $R_t = R_K$ , which introduces an implicit dependence on  $\omega$  into equation 8);

(v) finally, although not shown in the figures, the increase in the width of 2-m light minima toward more-rapid rotation.

At a quantitative level, the agreement between the two models is more limited. For instance, at large  $\beta$ , the torus model predicts an extension of the 2-m region to low inclinations, which is not seen in the RRM model. [In this particular case, the discrepancy arises because high- $\beta$  magnetospheres are punctured by cone-shaped voids over the rotational poles (see TO-05, fig. 3), and therefore do not produce light variations when viewed from low inclinations.] Such discrepancies mean that the torus model should not be used as the sole basis for data analysis. However, the points above are ample proof that – as a tool for data interpretation – the model has many useful insights to offer.

## 4 DISCUSSION

### 4.1 Photometric diagnostics

It has been demonstrated that the light variations arising from a RRM depend on fundamental stellar parameters in a way that is simple, regular and straightforward to understand. Given these qualities, it is reasonable to conjecture that observations of these variations in He-strong stars and similar objects could be used in tandem with other diagnostics, such as magnetic field measurements, to establish constraints on the parameters of these stars.

The success of this endeavour rests to a large part on the validity of the RRM model, as it is from diagrams such as Fig. 3 – constructed

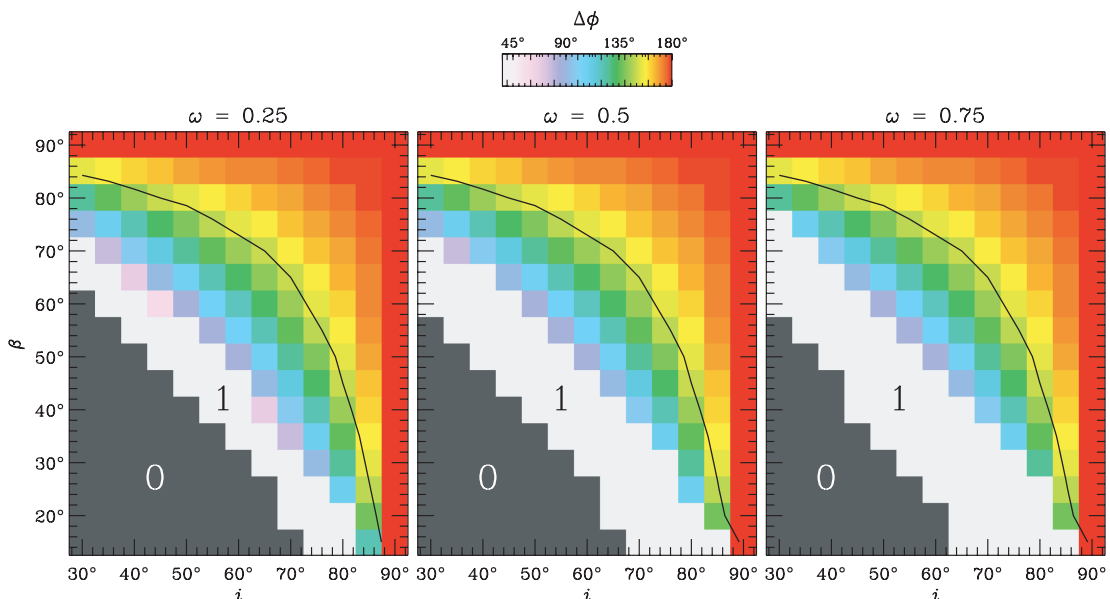


**Figure 7.** As for Fig. 3, except that the light curves are calculated using the torus model rather than the RRM model; in every case,  $d_t = 0.1R_*$ .

with the aid of the model – that reliable diagnostics are developed. In this respect, the close correspondence between the observed and synthesized H $\alpha$  variations of  $\sigma$  Ori E (Townsend et al. 2005) has lent considerable empirical support to the model. Moreover, recent rigid-field hydrodynamical simulations by Townsend, Owocki & ud-Doula (2007), and magnetohydrodynamical simulations by ud-Doula, Owocki & Townsend (2008) have provided confirmation of the theoretical underpinnings of the model.

Of equal importance, however, is the problem of disentangling the light variations arising from photospheric abundance inhomogeneities on the one hand, and from magnetospheric plasma on the other. For certain configurations, these two mechanisms can produce variability that appears ostensibly the same. For instance, the  $\{i, \beta\} = \{70^\circ, 20^\circ\}$  magnetospheric light curve in Fig. 1, showing a single, broad minimum, might easily be confused with the rotational modulation arising from a spot-like photospheric inhomogeneity. In situations like these, other diagnostics such as spectroscopy or polarimetry must be used to lift the degeneracy and correctly identify which mechanism is responsible for the observed variability.

In the majority of cases, however, the morphologies of the light curves produced by the alternative mechanisms are quite different. Especially toward large  $i$  and/or  $\beta$ , the light variations caused by magnetospheric plasma tend to be much more rapid (relative to the rotation period) than could plausibly be achieved by photospheric inhomogeneities. Thus, as a simple rule, faster variations can be attributed to the magnetosphere, and slower variations to the photosphere. By way of illustration, in Section 4.2 this heuristic is applied to five He-strong stars, in some cases examining whether the constraints provided by Fig. 3 are consistent with literature values for the parameters of these stars, and in other cases using such constraints to make predictions.

## 4.2 Application to He-strong stars

### 4.2.1 HD 37017

The light variations of this star (e.g. Bolton et al. 1998) show a smooth, sinusoidal character, favouring a photospheric rather than magnetospheric origin. Bohlender et al. (1987) derive  $42^\circ \lesssim \beta \lesssim 59^\circ$  and  $23^\circ \lesssim i \lesssim 37^\circ$  from magnetic and period measurements. With reference to Fig. 3, these values mostly fall in the 0-m region and are therefore consistent with the apparent lack of a magnetospheric signature.

### 4.2.2 HD 37479 ( $\sigma$ Ori E)

As already discussed in Section 1, this star exhibits distinctive 2-m light variations that are consistent with a magnetospheric origin. That said, certain aspects of its light curve, such as the unequal depths of the minima and the ‘emission’ feature after the secondary minimum, appear more likely to be of photospheric origin (see Townsend et al. 2005; note that these authors explained the depth asymmetry by instead invoking a decentred dipole).

Nevertheless, this photospheric signal is unlikely to have much effect on the measured phase difference  $\Delta\phi \approx 150^\circ$  between the two minima. This value is indicated in each panel of Fig. 3 by the contour curves. Along these contours, the combined angle  $\beta + i$  varies between  $\sim 105^\circ$  and  $\sim 135^\circ$ , which led Townsend et al. (2005) to adopt the approximate relation  $\beta + i \approx 130^\circ$  in developing their model for the star. This constraint is consistent with the parameters  $\{i, \beta\} \approx \{70^\circ, 56^\circ\}$  derived by Shore & Brown (1990) from

consideration of magnetic and *International Ultraviolet Explorer* data.

### 4.2.3 HD 37776

This star has a rather non-sinusoidal light curve, with a single, very broad minimum suggestive of a photospheric origin. Detailed modelling by Krtićka et al. (2007) demonstrates that, indeed, the photospheric abundance distribution determined spectroscopically by Khokhlova et al. (2000) can also faithfully reproduce the star’s light curve. Note that the star has a quadrupolar field topology (Thompson & Landstreet 1985). Although the RRM model can in principle be applied to any arbitrary field topology, studies so far (including the present paper) focus on the simplest and commonest case of a dipole field. Thus, the absence of a clear magnetospheric signature in the light curve of HD 37776 cannot, without further modelling, be used to constrain  $i$  or  $\beta$ .

### 4.2.4 HD 64740

This star is the brightest in the He-strong class, yet it exhibits almost no photometric variations (Pedersen & Thomsen 1977). Bohlender et al. (1987) derive  $\beta \lesssim 76^\circ$  and  $i \gtrsim 41^\circ$  from magnetic and period measurements. Given the absence of any variability, the boundary between the 0-m and 1-m regions in Fig. 3 (assuming  $\omega = 0.5$ ) can be used to further constrain the parameters as  $\beta + 2i \lesssim 150^\circ$ .

### 4.2.5 HD 182180

This star has recently been shown to be He-strong, and to exhibit H $\alpha$  and photometric variations, by Rivinius et al. (2008). Observational data remain scarce, but the 2-m,  $\Delta\phi = 180^\circ$  morphology of the double-wave light curve is consistent with  $\beta = 90^\circ$  and/or  $i = 90^\circ$ . The light minima are rather too broad to convincingly rule out a photospheric origin, but given the star’s extreme rotation period of 0.521 d, the widths of the minima are wholly consistent with a near-critical,  $\omega \approx 1$  configuration.

## 5 SUMMARY

The RRM model has been used to explore how the light variations due to magnetospheric plasma depend on the parameters  $\beta$ ,  $i$ ,  $\omega$  and  $\tau_0$  (Section 2). 2-m morphologies are found toward large values of the inclination  $i$  and/or obliquity  $\beta$ ; 1-m and 0-m morphologies occur for progressively smaller values of these parameters. In the 2-m cases, the phase difference  $\Delta\phi$  between the minima depends primarily on  $i$  and  $\beta$ , with almost no sensitivity to the rotation rate  $\omega$  or optical depth scale  $\tau_0$ .

Insight into these findings has been developed with the aid of an analytical torus model (Section 3). Although not in complete quantitative agreement with the RRM model, the torus model is able to explain all of the qualitative results from the parameter-space exploration. Applying these results, constraints on the obliquity and inclination of selected He-strong stars are derived from their light curves (Section 4); these are found to be generally consistent with values quoted in the literature.

## ACKNOWLEDGMENTS

I acknowledge support from the National Aeronautics and Space Administration (NASA) Long Term Space Astrophysics grant

NNG05GC36G. Interesting conversations with Stan Owocki, John Landstreet, Tom Bolton and Myron Smith provided much of the motivation to follow this line of research.

## REFERENCES

- Bohlender D. A., Landstreet J. D., 1988, in Cayrel de Strobel G., Spite M., eds, Proc. IAU Symp. 132, The Impact of Very High S/N Spectroscopy on Stellar Physics. Kluwer, Dordrecht, p. 309
- Bohlender D. A., Landstreet J. D., Brown D. N., Thompson I. B., 1987, *ApJ*, 323, 325
- Bolton C. T., Harmanec P., Lyons R. W., Odell A. P., Pyper D. M., 1998, *A&A*, 337, 183
- Groote D., Hunger K., 1982, *A&A*, 116, 64
- Hesser J. E., Walborn N. R., Ugarte P. P., 1976, *Nat*, 262, 116
- Hesser J. E., Ugarte P. P., Moreno H., 1977, *ApJ*, 216, L31
- Hunger K., Groote D., 1999, *A&A*, 351, 554
- Khokhlova V. L., Vasilchenko D. V., Stepanov V. V., Romanyuk I. I., 2000, *Astron. Lett.*, 26, 177
- Krtička J., Mikuláček Z., Zverko J., Žižňovský J., 2007, *A&A*, 470, 1089
- Michaud G., 1970, *ApJ*, 160, 641
- Osmer P. S., Peterson D. M., 1974, *ApJ*, 187, 117
- Pedersen H., 1979, *A&AS*, 35, 313
- Pedersen H., Thomsen B., 1977, *A&AS*, 30, 11
- Rivinius T., Štefl S., Townsend R. H. D., Baade D., 2008, *A&A*, 482, 255
- Shore S. N., Brown D. N., 1990, *ApJ*, 365, 665
- Thompson I. B., Landstreet J. D., 1985, *ApJ*, 289, L9
- Townsend R. H. D., Owocki S. P., 2005, *MNRAS*, 357, 251 (TO-05)
- Townsend R. H. D., Owocki S. P., Groote D., 2005, *ApJ*, 630, L81
- Townsend R. H. D., Owocki S. P., ud-Doula A., 2007, *MNRAS*, 382, 139
- Veto B., 1990, *Ap&SS*, 174, 111
- ud-Doula A., Owocki S. P., Townsend R. H. D., 2008, *MNRAS*, 385, 97
- Walborn N. R., Hesser J. E., 1976, *ApJ*, 205, L87

## APPENDIX A: DISC TILT ANGLE

As discussed in Section 1, the RRM model predicts magnetospheres that resemble a warped disc. A characteristic disc tilt angle  $\nu$  with respect to the rotation axis can be obtained by considering the locus formed by the minima of the dimensionless effective potential:

$$\Psi = -\frac{1}{\gamma \sin^2 \tilde{\theta}} - \frac{\gamma^2 \sin^4 \tilde{\theta}}{2} \times [\sin^2 \tilde{\theta} \sin^2 \tilde{\phi} + (\sin \beta \cos \tilde{\theta} + \cos \beta \sin \tilde{\theta} \cos \tilde{\phi})^2] \quad (\text{A1})$$

(cf. TO-05, equation 22). Here,  $\tilde{\theta}$  is the magnetic colatitude on the dipole field line having summit radius  $\gamma$  (in units of the Kepler radius  $R_K$ ; cf. equation 4) and magnetic azimuth  $\tilde{\phi}$ .<sup>2</sup> The conditions

<sup>2</sup> Not to be confused with the rotational phase  $\phi$ .

for a potential minimum are that

$$\frac{\partial \Psi}{\partial \tilde{\theta}} = 0, \quad \frac{\partial^2 \Psi}{\partial \tilde{\theta}^2} > 0. \quad (\text{A2})$$

As discussed by TO-05, an algebraic solution of these equations for general  $\beta$ ,  $\gamma$  and  $\tilde{\phi}$  is not possible. However, the  $\tilde{\phi} = 90^\circ, 270^\circ$  meridional planes are exceptions; for these, it is straightforward to demonstrate that minima occur at the magnetic equator,  $\tilde{\theta} = 90^\circ$ .

Immediately adjacent to these special cases, for instance in the  $\tilde{\phi} = 90^\circ + \delta_\phi$  meridional plane for  $|\delta_\phi| \ll 1$ , the continuity of the disc requires that the potential minimum should be at  $\tilde{\theta} = 90^\circ + \delta_\theta$ , where  $|\delta_\theta| \ll 1$  also. Substituting this trial solution into the zero-gradient condition in equation (A2), and neglecting terms of quadratic- or higher-order in  $\delta_\phi$  and  $\delta_\theta$ , leads to the equation

$$-\frac{\gamma^2 \sin 2\beta}{2} \tilde{\delta}_\phi + \left[ -\frac{2}{\gamma} + \frac{\gamma^2(5 + \cos 2\beta)}{2} \right] \tilde{\delta}_\theta = 0. \quad (\text{A3})$$

For field lines extending far outside the Kepler radius (i.e.  $\gamma \gg 1$ ), the solution is then found as

$$\tilde{\delta}_\theta = \frac{\sin 2\beta}{5 + \cos 2\beta} \tilde{\delta}_\phi. \quad (\text{A4})$$

The local tilt angle  $\tilde{\nu}$  of the disc with respect to the magnetic axis is determined from

$$\tan \tilde{\nu} = -\frac{\tilde{\delta}_\theta}{\tilde{\delta}_\phi} = -\frac{\sin 2\beta}{5 + \cos 2\beta}. \quad (\text{A5})$$

Thus, the tilt angle with respect to the rotational axis follows as

$$\nu = \beta + \tilde{\nu} = \beta - \tan^{-1} \left( \frac{\sin 2\beta}{5 + \cos 2\beta} \right). \quad (\text{A6})$$

Strictly speaking, this value cannot be applied across the whole of an RRM disc, because of the warping that arises when  $\beta > 0^\circ$ . However, as can be seen from fig. 3 of TO-05, the disc tilt in the  $\tilde{\phi} = 90^\circ, 270^\circ$  meridional planes furnishes a good approximation to the mean disc tilt, and therefore is well suited to characterizing the overall disc orientation.

This paper has been typeset from a  $\text{\TeX}/\text{\LaTeX}$  file prepared by the author.